

Lorentz drift compensation in high harmonic generation in the soft and hard X-ray regions of the spectrum

BENJAMIN R. GALLOWAY,^{1,*} DIMITAR POPMINTCHEV,¹ EMILIO PISANTY,^{2,3}
DANIEL D. HICKSTEIN,¹ MARGARET M. MURNANE,¹ HENRY C. KAPTEYN¹
AND TENIO POPMINTCHEV¹

¹JILA and Department of Physics, University of Colorado and NIST, Boulder, Colorado 80309-0440, USA

²Blackett Laboratory, Imperial College London, South Kensington Campus, SW7 2AZ London, UK

³Max Born Institute for Nonlinear Optics and Short Pulse Spectroscopy, Max Born Strasse 2a, 12489 Berlin, Germany

*benjamin.r.galloway@colorado.edu

Abstract: We present a semi-classical study of the effects of the Lorentz force on electrons during high harmonic generation in the soft and hard X-ray regions driven by near- and mid-infrared lasers with wavelengths from 0.8 to 20 μm , and at intensities below 10^{15} W/cm^2 . The transverse extent of the longitudinal Lorentz drift is compared for both Gaussian focus and waveguide geometries. Both geometries exhibit a longitudinal electric field component that cancels the magnetic Lorentz drift in some regions of the focus, once each full optical cycle. We show that the Lorentz force contributes a super-Gaussian scaling which acts in addition to the dominant high harmonic flux scaling of $\lambda^{(5-6)}$ due to quantum diffusion. We predict that the high harmonic yield will be reduced for driving wavelengths $> 6 \mu\text{m}$, and that the presence of dynamic spatial mode asymmetries results in the generation of both even and odd harmonic orders. Remarkably, we show that under realistic conditions, the recollision process can be controlled and does not shut off completely even for wavelengths $> 10 \mu\text{m}$ and recollision energies greater than 15 keV.

© 2016 Optical Society of America

OCIS codes: (190.2620) Harmonic generation and mixing; (320.7140) Ultrafast processes in fibers; (140.7240) UV, EUV, and X-ray lasers; (340.7480) X-rays, soft x-rays, extreme ultraviolet (EUV).

References and links

1. A. McPherson, G. Gibson, H. Jara, U. Johann, T. S. Luk, I. A. McIntyre, K. Boyer, and C. K. Rhodes, “Studies of multiphoton production of vacuum-ultraviolet radiation in the rare gases,” *J. Opt. Soc. Am. B* **4**(4), 595–601 (1987).
2. J. L. Krause, K. J. Schafer, and K. C. Kulander, “High-Order Harmonic Generation from Atoms and Ions in the High Intensity Regime,” *Phys. Rev. Lett.* **68**(24), 3535–3538 (1992).
3. P. B. Corkum, “Plasma Perspective on Strong Field Multiphoton Ionization,” *Phys. Rev. Lett.* **71**(13), 1994–1997 (1993).
4. M. Lewenstein, P. Balcou, M. Y. Ivanov, A. L’Huillier, and P. B. Corkum, “Theory of high-harmonic generation by low-frequency laser fields,” *Phys. Rev. A* **49**(3), 2117–2132 (1994).
5. C. G. Durfee III, A. R. Rundquist, S. Backus, C. Herne, M. M. Murnane, and H. C. Kapteyn, “Phase Matching of High-Order Harmonics in Hollow Waveguides,” *Phys. Rev. Lett.* **83**(11), 2187–2190 (1999).
6. H. C. Kapteyn, M. M. Murnane, and I. P. Christov, “Extreme Nonlinear Optics : Coherent X Rays from Lasers,” *Phys. Today* **58**(3), 39–46 (2005).
7. C. Hernández-García, J. A. Pérez-Hernández, T. Popmintchev, M. M. Murnane, H. C. Kapteyn, A. Jaron-Becker, A. Becker, and L. Plaja, “Zeptosecond High Harmonic keV X-Ray Waveforms Driven by Midinfrared Laser Pulses,” *Phys. Rev. Lett.* **111**(3), 033002 (2013).
8. T. Popmintchev, M.-C. Chen, D. Popmintchev, P. Arpin, S. Brown, S. Ališauskas, G. Andriukaitis, T. Balčiūnas, O. D. Mücke, A. Pugzlys, A. Baltuška, B. Shim, S. E. Schrauth, A. Gaeta, C. Hernández-García, L. Plaja, A. Becker, A. Jaron-Becker, M. M. Murnane, and H. C. Kapteyn, “Bright Coherent Ultrahigh Harmonics in the keV X-ray Regime from Mid-Infrared Femtosecond Lasers,” *Science* **336**(6086), 1287–1291 (2012).
9. J. Tate, T. Auguste, H. G. Muller, P. Salières, P. Agostini, and L. F. DiMauro, “Scaling of Wave-Packet Dynamics in an Intense Midinfrared Field,” *Phys. Rev. Lett.* **98**(1), 013901 (2007).

10. J. A. Pérez-Hernández, L. Roso, and L. Plaja, "Harmonic generation beyond the Strong-Field Approximation: the physics behind the short-wave-infrared scaling laws," *Opt. Express* **17**(12), 9891–9903 (2009).
11. M. V. Frolov, N. L. Manakov, and A. F. Starace, "Wavelength Scaling of High-Harmonic Yield: Threshold Phenomena and Bound State Symmetry Dependence," *Phys. Rev. Lett.* **100**(17), 173001 (2008).
12. T. Popmintchev, M.-C. Chen, A. Bahabad, M. Gerrity, P. Sidorenko, O. Cohen, I. P. Christov, M. M. Murnane, and H. C. Kapteyn, "Phase matching of high harmonic generation in the soft and hard X-ray regions of the spectrum," *Proc. Natl. Acad. Sci. U.S.A.* **106**(26), 10516–10521 (2009).
13. Q. Lin, S. Li, and W. Becker, "High-order harmonic generation in a tightly focused laser beam," *Opt. Lett.* **31**(14), 2163–2165 (2006).
14. M. Verschl, "Laser-Driven Recollisions Generalized to Relativistic Energies," *Laser Phys.* **18**(5), 598–607 (2008).
15. B. Henrich, K. Z. Hatsagortsyan, and C. H. Keitel, "Positronium in Intense Laser Fields," *Phys. Rev. Lett.* **93**(1), 013601 (2004).
16. N. Milosevic, P. B. Corkum, and T. Brabec, "How to Use Lasers for Imaging Attosecond Dynamics of Nuclear Processes," *Phys. Rev. Lett.* **92**(1), 013002 (2004).
17. A. V. Kim, M. Yu. Ryabikin, and A. M. Sergeev, "From femtosecond to attosecond pulses," *Usp. Fiz. Nauk* **169**, 58–66 (1999), *Phys. Uspekhi* **42**(1), 54–61 (1999).
18. S. Palaniyappan, I. Ghebrezabher, A. DiChiara, J. MacDonald, and B. Walker, "Emergence from nonrelativistic strong-field rescattering to ultrastrong-field laser-atom physics: A semiclassical analysis," *Phys. Rev. A* **74**(3), 033403 (2006).
19. C. C. Chirilă, N. J. Kylstra, R. M. Potvliege, and C. J. Joachain, "Nondipole effects in photon emission by laser-driven ions," *Phys. Rev. A* **66**(6), 063411 (2002).
20. T. Popmintchev, "Tunable Ultrafast Coherent Light in the Soft and Hard X-ray Regions of the Spectrum : Phase Matching of Extreme High-Order Harmonic Generation," PhD. Thesis, University of Colorado (2009).
21. A. Ludwig, J. Maurer, B. W. Mayer, C. R. Phillips, L. Gallmann, and U. Keller, "Breakdown of the Dipole Approximation in Strong-Field Ionization," *Phys. Rev. Lett.* **113**(24), 243001 (2014).
22. L. Cicchitelli, H. Hora, and R. Postle, "Longitudinal field components for laser beams in vacuum," *Phys. Rev. A* **41**(7), 3727–3732 (1990).
23. E. A. J. Marcatili and R. A. Schmeltzer, "Hollow Metallic and Dielectric Waveguides for Long Distance Optical Transmission and Lasers," *Bell Syst. Tech. J.* **43**(4), 1783–1809 (1964).
24. T. Ditmire, K. Kulander, J. K. Crane, H. Nguyen, and M. D. Perry, "Calculation and measurement of high-order harmonic energy yields in helium," *J. Opt. Soc. Am. B* **13**(2), 406–411 (1996).
25. B. Walker, B. Sheehy, K. C. Kulander, and L. F. DiMauro, "Elastic Rescattering in the Strong Field Tunneling Limit," *Phys. Rev. Lett.* **77**(25), 5031–5034 (1996).
26. B. Walker, B. Sheehy, L. F. DiMauro, P. Agostini, K. J. Schafer, and K. C. Kulander, "Precision Measurement of Strong Field Double Ionization of Helium," *Phys. Rev. Lett.* **73**(9), 1227–1230 (1994).
27. D. D. Hickstein, P. Ranitovic, S. Witte, X.-M. Tong, Y. Huismans, P. Arpin, X. Zhou, K. E. Keister, C. W. Hogle, B. Zhang, C. Ding, P. Johnsson, N. Toshima, M. J. J. Vrakking, M. M. Murnane, and H. C. Kapteyn, "Direct Visualization of Laser-Driven Electron Multiple Scattering and Tunneling Distance in Strong-Field Ionization," *Phys. Rev. Lett.* **109**(7), 073004 (2012).
28. E. Pisanty and M. Ivanov, "High harmonic interferometry of the Lorentz force in strong mid-infrared laser fields," <https://arxiv.org/abs/1606.01931>.
29. R. Abrams, "Coupling losses in hollow waveguide laser resonators," *IEEE J. Quantum Electron.* **8**(11), 838–843 (1972).
30. M. Y. Ivanov, T. Brabec, and N. Burnett, "Coulomb corrections and polarization effects in high-intensity high-harmonic emission," *Phys. Rev. A* **54**(1), 742–745 (1996).
31. M.-C. Chen, C. Mancuso, C. Hernández-García, F. Dollar, B. Galloway, D. Popmintchev, P.-C. Huang, B. Walker, L. Plaja, A. A. Jaroñ-Becker, A. Becker, M. M. Murnane, H. C. Kapteyn, and T. Popmintchev, "Generation of bright isolated attosecond soft X-ray pulses driven by multicycle midinfrared lasers," *Proc. Natl. Acad. Sci. U.S.A.* **111**(23), E2361–E2367 (2014).
32. K. T. Kim, C. Zhang, A. D. Shiner, S. E. Kirkwood, E. Frumker, G. Gariepy, A. Naumov, D. M. Villeneuve, and P. B. Corkum, "Manipulation of quantum paths for space – time characterization of attosecond pulses," *Nat. Phys.* **9**(3), 159–163 (2013).
33. O. Cohen, A. L. Lytle, X. Zhang, M. M. Murnane, and H. C. Kapteyn, "Optimizing quasi-phase matching of high harmonic generation using counterpropagating pulse trains," *Opt. Lett.* **32**(20), 2975–2977 (2007).
34. X. Zhang, A. L. Lytle, T. Popmintchev, X. Zhou, H. C. Kapteyn, M. M. Murnane, and O. Cohen, "Quasi-phase-matching and quantum-path control of high-harmonic generation using counterpropagating light," *Nat. Phys.* **3**(4), 270–275 (2007).
35. X. P. Hu, P. Xu, and S. N. Zhu, "Engineered quasi-phase-matching for laser techniques," *Photon. Res.* **1**(4), 171–185 (2013).

1. Introduction

High harmonic generation (HHG) is an extreme nonlinear response of atoms to intense femtosecond laser fields, which makes it possible to upconvert ultraviolet, visible, and

infrared (IR) laser light to much higher photon energies. In HHG, atoms undergo tunnel ionization in the strong driving laser field, and the resulting electrons are accelerated by the field before recombining with their parent ion to emit harmonics [1–7]. The harmonic cutoff photon energy for a single atom is given by $\hbar\nu_{\text{SAcutoff}} = I_p + 3.17 U_p$, where \hbar is Planck's constant, ν_{SAcutoff} is the frequency of the cutoff harmonic, I_p is the ionization potential of the target gas, and for a driving laser with intensity I_L and wavelength λ_L , $U_p \propto I_L \lambda_L^2$ is the quiver energy of the electron in the field. As a result, one route for achieving higher HHG photon energies is to increase the driving laser wavelength. However, past studies have suggested that this approach would adversely affect the HHG flux, since theory predicts a single-atom fluence scaling of $\lambda_L^{-(5-6)}$ due to quantum diffusion of the electron wavepacket [8–11]. Fortunately, in recent work using mid-IR driving lasers, we demonstrated that phase-matched growth in very high pressure gases can compensate for the low single atom HHG yield. Thus, bright HHG beams can be produced up to photon energies >1.6 keV, corresponding to >5,000 harmonic orders [8, 12]. However, a classical picture of electron trajectories following ionization predicts that for significantly longer wavelengths than those used experimentally to date (up to 4 μm), the Lorentz $\mathbf{v} \times \mathbf{B}$ force will cause the electron to miss its parent ion, avoiding recollision and shutting-off the HHG process.

In this paper, we present a semi-classical study of the influence of the Lorentz force on electron trajectories during high harmonic generation driven by near- and mid-infrared lasers with wavelengths from 0.8 to 20 μm, and at optimal intensities up to 10^{15} W/cm². Specifically, we investigate the longitudinal deflection induced by the Lorentz $\mathbf{v} \times \mathbf{B}$ force combined with the longitudinal component of the electric field of a confined laser focus, to show how the overall displacement depends on the driving laser wavelength, intensity, mode size, and HHG geometry. Previous studies of Lorentz drift effects focused on laser-matter interactions in ultra-intense fields ($>10^{15}$ W/cm²) that produce large ionization levels that are impractical for efficient, phase-matched HHG [13–19]. Here we investigate intensities relevant for phase-matched HHG in helium gas [12, 20]. We also investigate the geometry most successful for soft X-ray HHG to date, a gas-filled hollow waveguide, and compare it with a free-focus gas cell/jet geometry. In both cases, we find that the longitudinal electric field at the focus can readily cancel the magnetic Lorentz drift. Furthermore, we find that the Lorentz deflection generally allows for brighter harmonics at higher photon energies in a waveguide geometry than in a free focus geometry. We show that the Lorentz force contributes an additional super-Gaussian scaling to the expected HHG flux scaling per atom of $\lambda_L^{-(5-6)}$. We predict that the high harmonic yield will begin to show these effects for driving wavelengths > 6 μm. Experimental signatures of the Lorentz drift include a reduction in HHG yield, spatial mode shaping, and the emergence of even harmonics. However, in contrast to a plane wave with a fully transverse electromagnetic field, under realistic conditions the HHG recollision process does not shut off completely - even for driving wavelengths >10 μm and recollision energies greater than 15 keV. Additionally, the driving laser mode size can be varied to control the Lorentz drift and resulting HHG efficiency.

In the following analysis, the polarization of the driving laser is assumed to be linear and aligned along the y-axis, while the propagation direction \mathbf{k} is along the z-axis, as illustrated in Fig. 1. Interactions between electrons and neighboring neutral atoms are neglected, since experimental evidence to date indicates that HHG buildup occurs coherently even at the very high (>40 atm) gas pressures required to generate bright keV X-ray HHG beams, despite the incoherent scattering events that would occur at such pressures [8]. Additionally, electron excursion lengths are assumed to be small compared to the laser mode size so that field gradients can be ignored. This assumption is justified since gradients induce a maximal 3% change in drift magnitudes for all cases considered here.

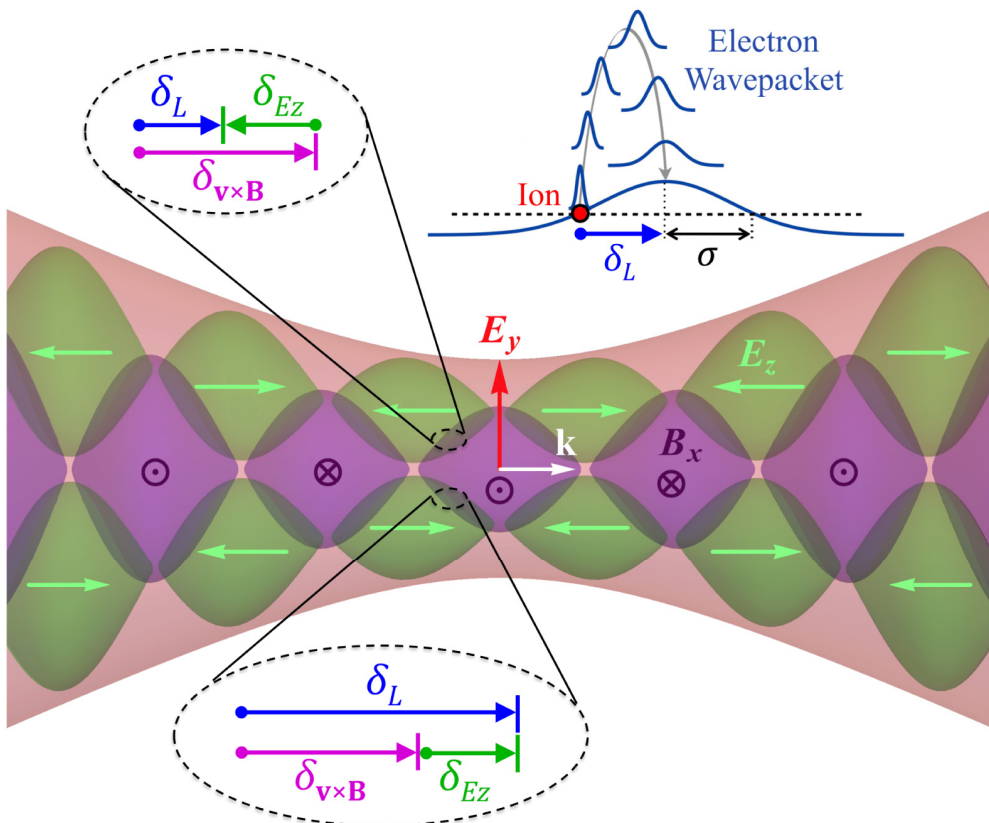


Fig. 1. Field components of a Gaussian free focus (in the waveguide case, the fields are similar but the guided beam does not diverge). The Gaussian mode envelope is depicted in red, the transverse fields E_y and B_x oscillate like the purple regions, and the longitudinal field E_z is depicted by the green regions. The longitudinal displacements due to the $\mathbf{v} \times \mathbf{B}$ force ($\delta_{v \times B}$), the longitudinal electric field (δ_{Ez}), and the total Lorentz force (δ_L) are shown in two locations in the focus, where the net displacement changes in magnitude. Top-right: Visualization of the electron wavepacket drift. Quantum diffusion of the electron wavepacket enables recollision in spite of significant Lorentz drift [7].

2. Lorentz drift derivation

In the classical three-step model [2, 3], an atom undergoes tunnel ionization at a time $t = 0$ and at a phase φ_0 measured with respect to the peak of the laser field. Depending on φ_0 , the electron may return to recombine with the ion ($y = 0$) at a later time τ_f , releasing a high harmonic photon with an energy that depends on I_p , U_p , and φ_0 . The probability of recombination P_R can be calculated through a quantum mechanical approach discussed in Section 3.

The laser-driven motion of the electron is primarily along the polarization axis of the laser field, as described in Eq. (1):

$$y(t) = \frac{-eE_L}{m_e\omega_L^2} [\omega_L t \sin(\varphi_0) + \cos(\omega_L t + \varphi_0) - \cos(\varphi_0)] \quad (1)$$

Here, $-e$ is the charge of electron, m_e is the electron mass, $\omega_L = 2\pi c / \lambda_L$ is the angular frequency of the laser, and E_L is the electric field magnitude of the laser ($I_L = \epsilon_0 c |E_L|^2 / 2$), with c the speed of light and ϵ_0 the vacuum permittivity.

In addition to the motion along the polarization direction, there is a smaller motion along the propagation axis due to two contributions from the Lorentz force. The first contribution arises due to the transverse magnetic field, leading to a force that is proportional to $\mathbf{v} \times \mathbf{B}$, or $v_y B_x$ to first order. Accounting for the fact that the transverse magnetic field magnitude $B_L \propto (E_L / c)$, the resulting motion along z due to the $\mathbf{v} \times \mathbf{B}$ force is given by Eq. (2):

$$z_{v \times B}(t) = \frac{e^2 E_L^2}{8 m_e^2 \omega_L^3 c} [4 \omega_L t - 2 \omega_L t \cos(2\varphi_0) - \sin(2\omega_L t + 2\varphi_0) - 4 \sin(\omega_L t) + 4 \sin(\omega_L t + 2\varphi_0) - 3 \sin(2\varphi_0)] \quad (2)$$

To determine the longitudinal displacement of the electron when it returns to the ($y=0$) plane, one simply evaluates $z_{v \times B}(t)$ for $t = \tau_f$. It is clear from Eq. (2) that the longitudinal drift associated with the $\mathbf{v} \times \mathbf{B}$ component of the Lorentz force scales as:

$$\delta_{v \times B} \propto \lambda_L^3 I_L \quad (3)$$

An important quality to note is that $\delta_{v \times B}$ will consistently point in the $+z$ direction, regardless of which $\frac{1}{2}$ -cycle the electron is ionized. This is due to the fact that $\delta_{v \times B} \propto v_y B_x$, and both v_y and B_x switch sign every $\frac{1}{2}$ -cycle [21].

The second contribution to the longitudinal motion arises from the longitudinal component of the electric field, which is typically neglected in this type of calculation since infinite plane wave TEM fields are often assumed ([13] is a notable exception). However, once a finite spatial mode of the driving laser is established, a longitudinal electric field component E_z arises that cannot be ignored, especially for tightly focused beams. The magnitude of E_z depends on the mode profile, but for a Gaussian focus [22] or EH₁₁ waveguide mode [23]: $E_z \propto E_L \lambda_L / w_L$, where w_L is the $1/e^2$ radius of the intensity profile. As depicted in Fig. 1, the E_z field varies spatially and has a phase offset of 90° with respect to the polarization component (E_y). Solving for the motion of the electron due to the E_z component, one obtains Eq. (4):

$$z_{Ez}(t) = \frac{-e E_z}{m_e \omega_L^2} [\omega_L t \cos(\varphi_0) - \sin(\omega_L t + \varphi_0) + \sin(\varphi_0)] \quad (4)$$

From the form of Eq. (4), and using the aforementioned scaling $E_z \propto E_L \lambda_L / w_L$, the longitudinal drift associated with E_z scales as:

$$\delta_{Ez} \propto \lambda_L^3 I_L^{1/2} w_L^{-1} \quad (5)$$

Unlike the drift from $\mathbf{v} \times \mathbf{B}$, the E_z drift switches sign every $\frac{1}{2}$ -cycle, which gives rise to spatio-temporal asymmetries discussed in Section 6.

For both longitudinal drifts, the scaling with τ_f , or more fundamentally φ_0 , cannot be described in a simple form; however, the magnitudes of these drifts generally decrease as φ_0

increases from 0 to $\pi/2$. The total longitudinal drift resulting from the Lorentz force will be the sum $\delta_L = \delta_{v \times B} + \delta_{Ez}$, and this quantity will vary spatially, as discussed in Section 5.

3. Recombination probability P_R

If the electron is treated classically, one would expect there to be greatly reduced probability for the electron to recombine with its parent ion if there is a longitudinal drift larger than a Bohr radius. However, due to the quantum nature of the electron, the electron wavepacket diffuses transversely as it travels in the continuum. Thus, for any finite spatial overlap between the diffused wavepacket ψ_d and the wavefunction of a bound electron ψ_b , the probability P_R of recombination and emission of a photon is nonzero and given by Eq. (6):

$$P_R = \int_{\mathbf{R}} d^3\mathbf{r} \psi_d^*(\mathbf{r}, t = \tau_f) \psi_b(\mathbf{r}) \quad (6)$$

One may also describe the harmonic yield as originating from a time-varying dipole moment, arising from the interference of $\psi_d(\mathbf{r}, t)$ with $\psi_b(\mathbf{r}, t)$. In either case, the photon yield will be proportional to P_R as well as the ionization rate at the time the electron was ionized $\Gamma(\mathbf{r}_0, t = 0)$ [4, 13, 24].

To approximate $\psi_d(\mathbf{r}, t)$, we use the Gaussian approximation used in [13, 18, 25]. Specifically, we approximate the wavepacket using the time-dependent form $\psi_d(\mathbf{r}, t) = \exp\{-r^2/[2\sigma(t)^2]\}$, where $\sigma(t) = \{\sigma(0)^2 + [2t/\sigma(0)]^2\}^{1/2}$. As in [25], we assume an initial electron wavepacket width of four Bohr radii, i.e. $\sigma(0) = 4a_0$. This assumption is physical since the laser field distorts the Coulomb potential of the ion, thereby perturbing the wavefunction of the bound electron before tunnel ionization occurs. The choice of $4a_0$ is consistent with more rigorous numerical studies and experimental observations [26, 27].

When $\psi_d(\mathbf{r}, t = \tau_f)$ is evaluated for even the shortest wavelength considered here (0.8 μm), it becomes evident that the integral describing P_R can be reduced. The diffused wavepacket $\psi_d(\mathbf{r}, \tau_f)$ returns with a width that is orders of magnitude larger than the width of $\psi_b(\mathbf{r})$. For the purposes of integration, $\psi_b(\mathbf{r})$ can be approximated as a delta function. Instead of applying the Lorentz drift δ_L to ψ_d , it is straightforward to apply it to ψ_b , representing it as a shifted delta function: $\psi_b(\mathbf{r}) = \delta(\mathbf{r} - \delta_L \hat{k})$. Considering only the wavefunction amplitude, the form of P_R can be rewritten: $P_R = |\psi_d(\delta_L, \tau_f)|$. Note that the drift-induced quantum phase dynamics of the electron can shift the absolute positions of the harmonic peaks in the spectral domain, but should not change the overall single-atom spectral shape [28]. Only amplitude effects will be considered here.

To determine how the Lorentz drift influences the high harmonic flux, a comparison must be made between the case when the Lorentz drift is included, and the case when it is set to zero. The relevant comparison is the ratio of recombination probabilities for the two cases, expressed as a recombination probability ratio (RPR) defined in Eq. (7):

$$\text{RPR} = P_R(\delta_L) / P_R(0) = \frac{|\psi_d(\delta_L, \tau_f)|}{|\psi_d(0, \tau_f)|} \quad (7)$$

The RPR is defined for a single electron ionized during a particular $1/2$ -cycle of the driving laser, and has a maximum value of 1 corresponding to zero displacement. In the following

Section, we quantify how this recombination probability ratio scales with wavelength, indicating a reduction in HHG fluence as the wavelength is increased.

4. Scaling of the recombination probability ratio with laser wavelength

In order to study Lorentz displacement effects under conditions applicable to HHG, the intensity of the driving laser must be chosen to achieve bright, phase-matched HHG flux. Constraining the intensity to the wavelength also simplifies the investigation by reducing the parameter space. We assume the target gas is helium and the peak intensity of the driver is optimized for maximal, mode-averaged, phase-matched HHG flux driven by an 8-cycle pulse, as calculated in [20]. With this assumption, and using reasonable values for the laser mode size, it becomes evident that the Lorentz displacement produces a non-negligible effect for wavelengths larger than $\sim 6 \mu\text{m}$. Table 1 summarizes the relevant wavelength-dependent parameters and the resulting displacements and RPR values. The net Lorentz drift magnitude $|\delta_L|$ varies across the transverse spatial dimensions, but a ‘symmetric’ net drift $|\delta_L|_{\text{symm}}$ can be defined at the location where $|\delta_{v\times B}|$ is the same magnitude as $|\delta_{Ez}|$. This ‘symmetric’ net drift is listed in Table 1, and provides a metric to estimate when the field-driven electrons will be displaced far enough to miss the ion during one $\frac{1}{2}$ -cycle, while trajectories during the next $\frac{1}{2}$ -cycle (when $\delta_{v\times B}$ and δ_{Ez} have opposite sign) directly recollide with the ion. It is important to note that δ_{Ez} has a magnitude $\geq \delta_{v\times B}$ when using the harmonic cutoff ionization phase $\phi_0 = 18^\circ$. Even when considering the Lorentz force in ultra-strong field experiments, the driving laser typically must be tightly focused to achieve relativistic intensities ($I_L > 10^{18} \text{ W/cm}^2$), in which case the contribution from E_z is large and cannot be ignored.

Table 1. Lorentz Displacement Results for Selected Laser Wavelengths^a

$\lambda_L [\mu\text{m}]$	$I_L [\times 10^{14} \text{ W/cm}^2]$	$ \delta_{v\times B} [\text{\AA}]$	$ \delta_{Ez} [\text{\AA}]$	$ \delta_L _{\text{symm}} [\text{\AA}]$	$\sigma(\tau_f) [\text{\AA}]$	RPR _{symm}
0.8	7.58	0.372	0.293	0.455	19.1	0.9997
3.0	4.20	10.9	11.5	15.0	71.1	0.9779
6.0	3.26	67.7	81.1	103	142	0.7671
8.0	2.97	146	183	223	189	0.5000
10.0	2.77	266	346	406	237	0.2298
15.0	2.45	794	1,100	1,213	355	0.0029
20.0	2.25	1,731	2,507	2,648	474	10^{-7}

^aThe driving laser mode is assumed to be $100 \mu\text{m}$ in diameter, and the ionization phase $\phi_0 = 18^\circ$. Maximum values within the spatial mode are presented for $|\delta_{v\times B}|$ and $|\delta_{Ez}|$, whereas $|\delta_L|_{\text{symm}}$ represents the total Lorentz displacement at the spatial location along the polarization axis where $|\delta_{v\times B}| = |\delta_{Ez}|$. The reported RPR values are for the same location.

Although we have previously derived a λ_L^3 scaling for each of the longitudinal drift components, the optimal intensity for HHG flux scales close to $\lambda_L^{-0.4}$. Thus, the final scaling of the total Lorentz drift will be close to $\lambda_L^{2.6}$. Figure 2 shows the magnitude of the net Lorentz drift $|\delta_L|_{\text{symm}}$ plotted as a function of wavelength, where its measured slope of 2.62 verifies the wavelength scaling. The width of ψ_d upon return to the parent ion $\sigma(\tau_f)$ scales linearly with wavelength, and is also plotted in Fig. 2. The inset of Fig. 2 shows the effect of $|\delta_L|_{\text{symm}}$ on the RPR for adjacent $\frac{1}{2}$ -cycles. For one of the $\frac{1}{2}$ -cycles $|\delta_{v\times B}|$ cancels $|\delta_{Ez}|$, whereas they add in the next $\frac{1}{2}$ -cycle. Thus, the RPR alternates between unity and RPR_{symm}.

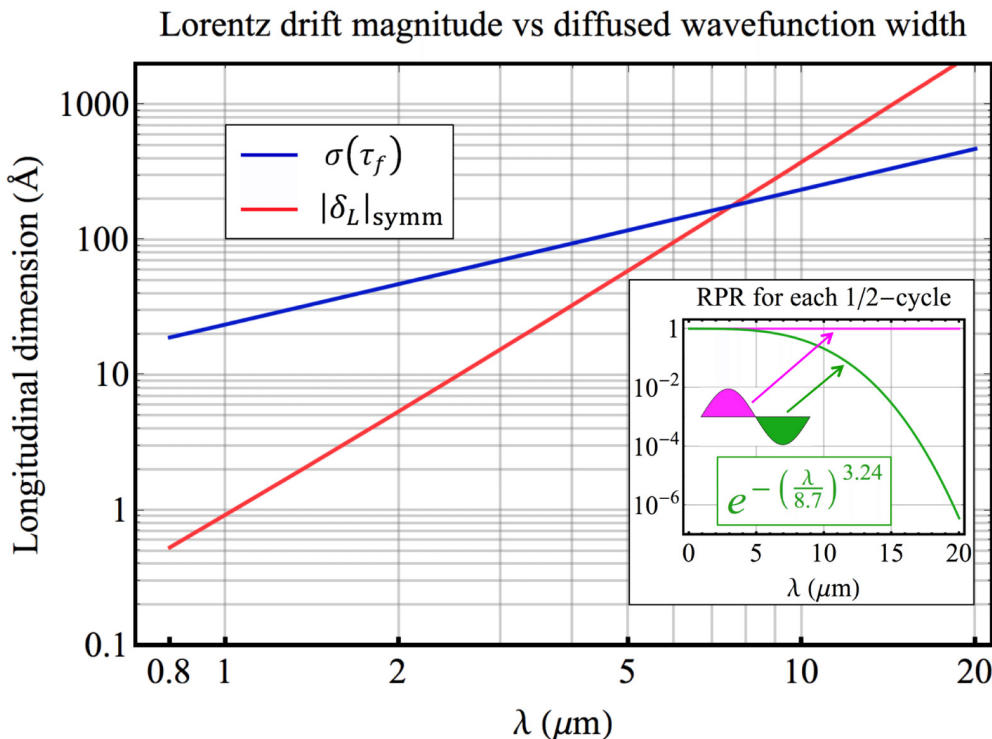


Fig. 2. Total Lorentz drift magnitude (red) and diffused electron wavepacket width (blue) as a function of driving laser wavelength. The electron is assumed to be ionized at 18° , and the laser intensities used are those that maximize phase-matched HHG flux in Helium. $|\delta_L|_{\text{symm}}$ is calculated at the spatial location along the polarization axis where $|\delta_{v \times B}| = |\delta_{Ez}|$. The lines intersect at $\lambda = 7.4 \mu\text{m}$ and 175\AA , after which the Lorentz drift exceeds the wavepacket width. The inset shows the RPR for adjacent $\frac{1}{2}$ -cycles where $|\delta_L|_{\text{symm}}$ is calculated, indicating a harmonic efficiency that is modulated in the time domain with λ -periodicity.

The Lorentz displacement increases at a rate $\lambda_L^{1.62}$ faster than the diffused wavepacket width. Accounting for the Gaussian form of ψ_d , the resulting scaling of the RPR, and the total HHG flux, is given by Eq. (8):

$$\text{RPR} \sim \exp\left[-\left(\frac{\delta_L}{\sigma}\right)^2\right] \sim \exp\left[-\left(\left(\frac{\lambda_L}{D}\right)^{1.62}\right)^2\right] \sim \exp\left[-\left(\frac{\lambda_L [\mu\text{m}]}{8.7}\right)^{3.24}\right] \quad (8)$$

The fitting parameter D was calculated to nicely fit the RPR trend using the data in Table 1. Fitting to the mode- and φ_0 -integrated RPR for harmonics $> 2 U_p$ causes the D parameter to increase to ~ 13.3 , with some underestimation at longer wavelengths. The super-Gaussian form of Eq. (8) encapsulates the initially slow onset of the Lorentz displacement, followed by a steep reduction of the RPR for $\lambda_L > 6 \mu\text{m}$. Note that this flux scaling only accounts for the Lorentz displacement and will act in addition to the $\lambda_L^{-(5-6)}$ scaling from quantum diffusion [8–11]. Interestingly, the flux attenuation due to quantum diffusion is dominant even up to $20 \mu\text{m}$ drivers, indicating that the Lorentz drift is not the limiting factor with respect to high harmonic flux driven by long wavelengths.

5. X-ray spatial profiles in Gaussian foci and in waveguides

In addition to attenuating the total high harmonic flux, the Lorentz displacement also has a spatial dependence that influences the HHG mode. For Gaussian foci, the electromagnetic field components described in Eqs. (13)-(17) from [22] are used. For hollow dielectric waveguides, the linearly-polarized EH₁₁ hybrid mode described in Eq. (4) of [23] is used. In both cases, the E_y and B_x components take a Gaussian or near-Gaussian form, while the E_z component has a two-lobed structure that arises from taking a spatial derivative of the E_y mode along the polarization axis; The E_z component is positive in one half of the mode, zero at the center, and negative in the other half, as illustrated in Fig. 1.

Figure 3 shows the Lorentz displacements and RPR profile using a Gaussian focus geometry for a single $\frac{1}{2}$ -cycle of a 10 μm driving laser, assuming the electron is ionized at the harmonic cutoff phase $\phi_0 = 18^\circ$. The energy of an emitted harmonic will be 3.17 times the local $U_{P,\text{loc}}$, which depends on the local intensity. This local energy can be rewritten in terms of the maximum harmonic energy $3.17 U_P$, occurring at the center of the mode where the intensity is the highest (I_L). In Fig. 3(d), rings are plotted where the local cutoff energies correspond to 1 and 2 times the maximum U_P . Note that the plots would be reflected about the x-axis for the next $\frac{1}{2}$ -cycle, due to the sign flip of δ_{Ez} but not $\delta_{v \times B}$.

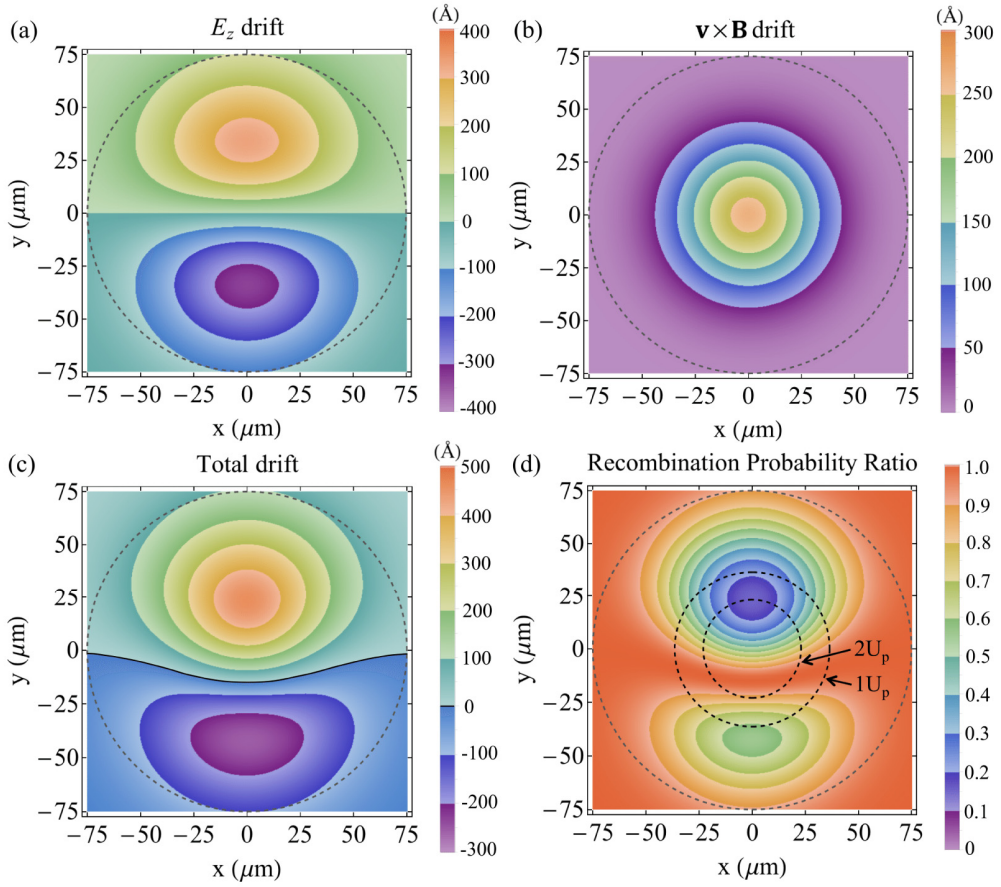


Fig. 3. Spatially-resolved Lorentz displacements and resulting recombination probability ratio (RPR) for a Gaussian focus with $\lambda_L = 10 \mu\text{m}$ ($I_L = 2.77 \times 10^{14} \text{ W/cm}^2$, $w_L = 50 \mu\text{m}$, $\varphi_0 = 18^\circ$). (a) δ_{E_z} , (b) $\delta_{v \times B}$, (c) δ_L , (d) RPR. The outer dashed circles represent the inside wall of a waveguide that this Gaussian mode would couple to optimally. The middle and inner dashed circles in (d) represent the radii within which $1U_p$ and $2U_p$ HHG can be generated, corresponding to 2.5 keV and 5.1 keV, respectively.

Figure 4 shows the same plots as Fig. 3, but for a waveguide geometry with an inside diameter (*I.D.*) resulting in an equivalent mode size ($2w_L = 0.64 \text{ I.D.}$) [29]. Note that the separate components of the Lorentz drift δ_{E_z} and $\delta_{v \times B}$ add in one half of the mode, while they cancel in the other half. While this is, from a flux perspective, detrimental for one half of the mode, the other half can benefit from the drift cancellation. If the flux for only the highest harmonics ($> 2U_p$) is to be optimized, the drift cancellation should occur as close to the center of the mode as possible. By definition, the E_z field is zero at the center, so its resulting drift cannot cancel the $v \times B$ drift, which is maximal at the center. To shift the location of drift cancellation closer to the center, one can simply inspect the drift scaling laws in Eq. (3) and Eq. (5) to conclude that the driving laser mode size should be reduced. By changing the relative magnitude of δ_{E_z} with respect to $\delta_{v \times B}$, one can control the spatial position of drift cancellation. In fact, by specifying a driving wavelength and constraining the intensity to be optimal for HHG, the only free parameter to control the RPR mode profile is the mode size.

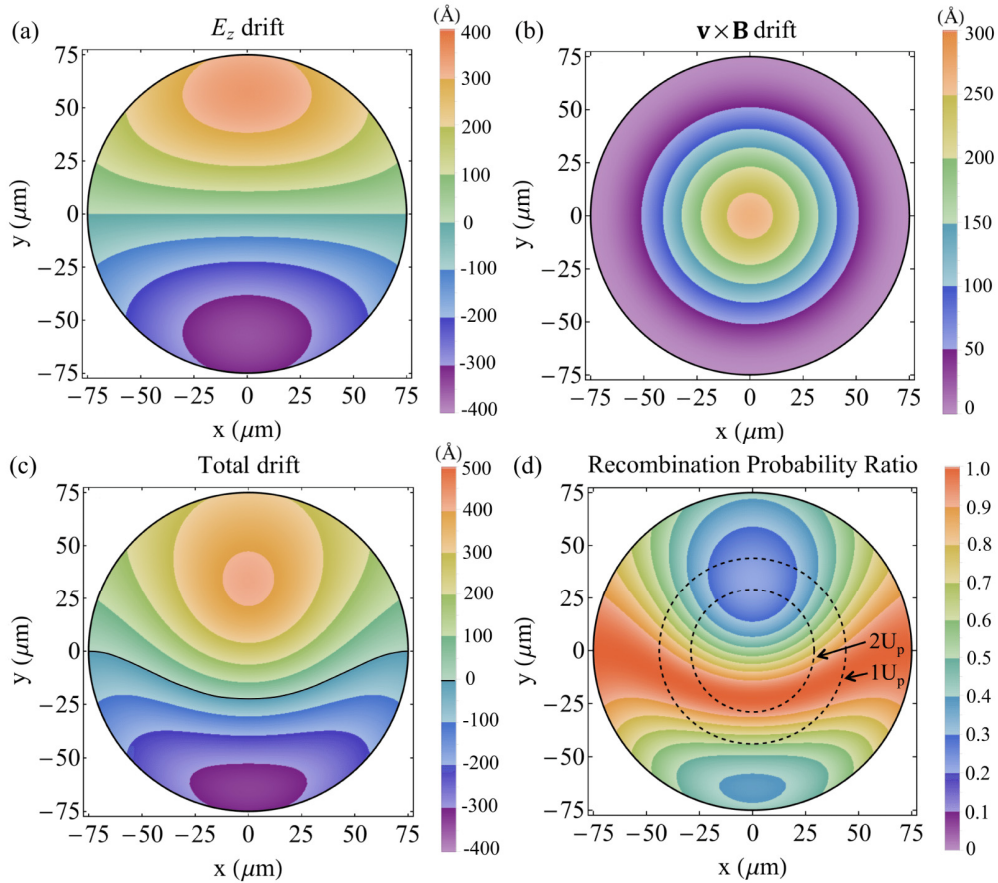


Fig. 4. Spatially-resolved Lorentz displacements and resulting recombination probability ratio (RPR) for a EH₁₁ waveguide mode with $\lambda_L = 10 \mu\text{m}$ ($I_L = 2.77 \times 10^{14} \text{ W/cm}^2$, I.D. = 150 μm , $\phi_0 = 18^\circ$). (a) δ_{Ez} , (b) $\delta_{v \times B}$, (c) δ_L , (d) RPR. The middle and inner dashed circles in (d) represent the radii within which $1U_p$ and $2U_p$ HHG are generated, corresponding to 2.5 keV and 5.1 keV, respectively.

In Fig. 5, the HHG photon energy at the location of drift cancellation is plotted as a function of wavelength and mode size. Generally, the RPR approaches unity at a higher harmonic energy in waveguides than in a Gaussian focus, for comparable mode sizes. For a 20 μm driver with optimal intensity of $2.77 \times 10^{14} \text{ W/cm}^2$ in a 250 μm I.D. waveguide, the HHG energy that has RPR = 1 is approximately $2U_p$, which is ≈ 17 keV. This shows that even very high energy harmonics in the hard X-ray region can be produced through HHG without the Lorentz drift shutting off the recollision process. Furthermore, Fig. 5 can be used as a guide to select the mode size necessary for drift cancellation and efficient generation of a desired HHG photon energy.

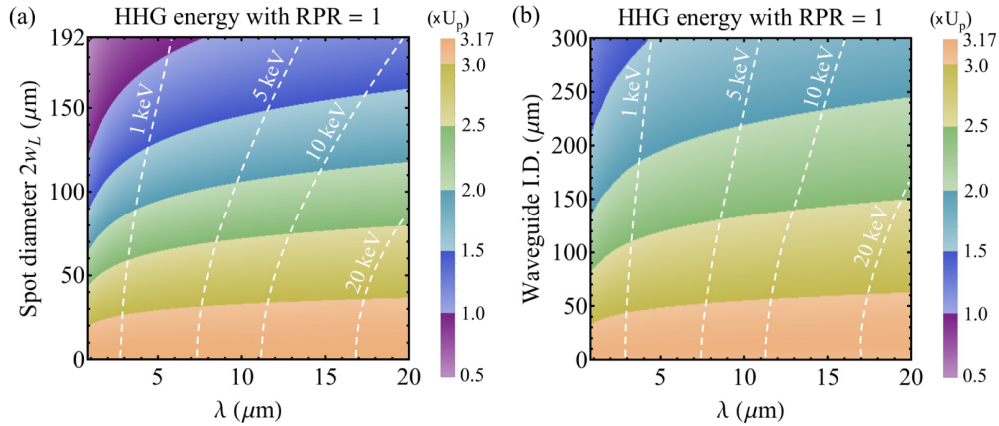


Fig. 5. Energy of the harmonic emitted at the location of drift cancellation, corresponding to RPR = 1. The color scale corresponds to energies in terms of the ponderomotive potential $U_p \propto I_L \lambda^2$, while the dashed lines indicate energy contours in keV. The cutoff ionization phase $\phi_0 = 18^\circ$ is used. The Gaussian focus geometry is shown in (a), while the waveguide geometry is shown in (b). The vertical axes of both plots give comparable mode sizes.

Although the single-phase harmonic cutoff results in Figs. 3-5 are informative, the total HHG mode emitted from a single $\frac{1}{2}$ -cycle would result from electrons ionized at all phases within $\{0, \pi/2\}$. Ionization phases closer to the peak of the field ($\phi_0 \sim 0$) have the highest ionization rate (Γ), but these electrons spend more time (τ_f) free from the parent and have a lower probability of recombining. For later phases, the low field strength results in reduced ionization rates, and thus, reduced harmonic emission. Performing a weighted integral of the recombination probability ratio over the entire phase range can provide an approximation of the total $\frac{1}{2}$ -cycle HHG mode. The appropriate weighting function $f(\phi_0)$ to incorporate the phase-dependent effects follows the harmonic yield scaling described in [30] Eqs. (5)-(7): $f(\phi_0) = \Gamma(\phi_0) \times \tau_f(\phi_0)^{-3} / E^2(\phi_0)$, where $\Gamma(\phi_0) \propto \exp[-\beta / E(\phi_0)]$, with β related to the ionization potential of the gas. Figure 6 shows the phase-integrated RPR for all harmonic energies in both the Gaussian focus (a) and waveguide (b) geometries. Figures 6(c) and 6(d) are identical to 6(a) and 6(b), but only HHG energies above $1U_p$ contribute. Primarily due to differences in mode shape, there is a larger area with nonzero RPR in Fig. 6(d) than in Fig. 6(c), indicating a mode-averaged flux advantage for the waveguide case over the Gaussian focus case. It is important to note that different ionization phases will have different spatial profiles for the individual drifts, and thus, the final RPR profile. As a result, different spectral regions will be emitted with different spatial modes, giving rise to complicated spectral-spatial dynamics when propagation and phase-matching are considered.

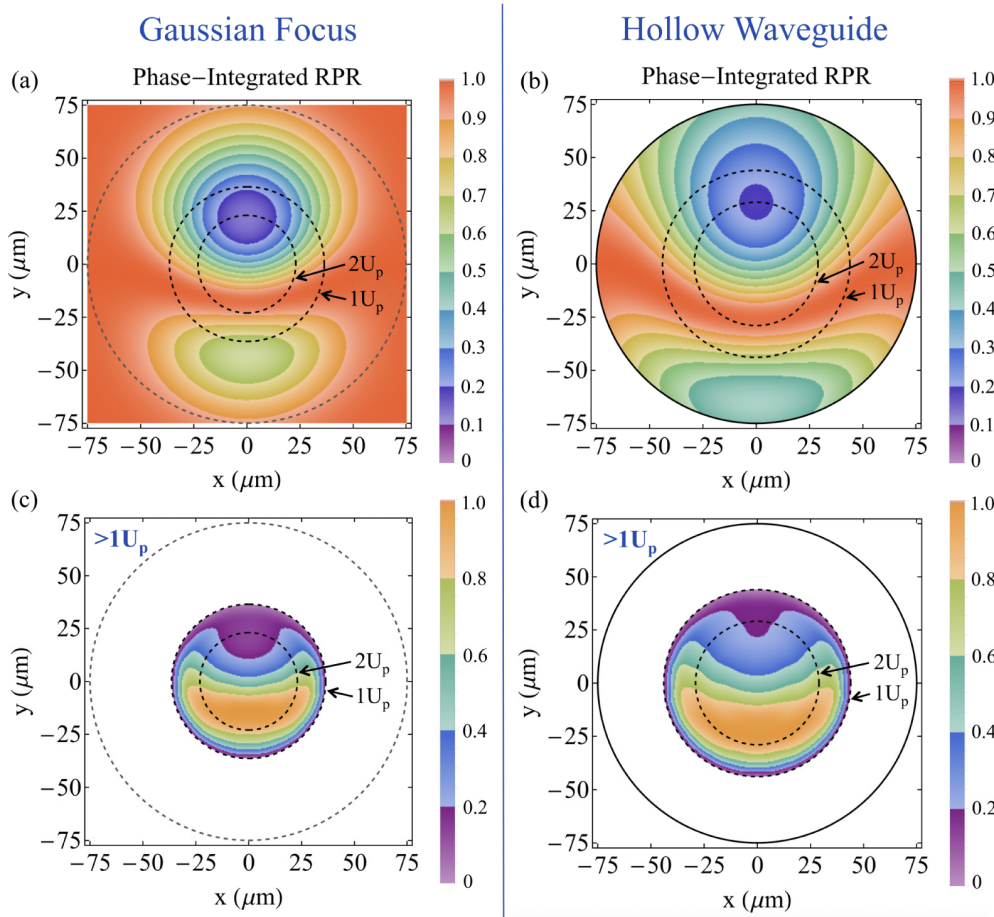


Fig. 6. Spatially-resolved, phase-integrated recombination probability ratio (RPR) for all harmonics vs plateau and cutoff harmonics. Plots (a) and (c) correspond to a Gaussian focus geometry, while plots (b) and (d) correspond to a waveguide geometry. All harmonic energies contribute in (a) and (b), while only energies above $1U_p$ contribute in (c) and (d). For all cases, the driving laser has wavelength $\lambda_L = 10 \mu\text{m}$, spot radius $w_L = 50 \mu\text{m}$ ($I.D. = 150 \mu\text{m}$), and peak intensity $I_L = 2.77 \times 10^{14} \text{ W/cm}^2$.

6. Experimental signatures of the Lorentz drift

There are a number of experimental indicators that can confirm the Lorentz drift effects predicted above. One of the most important challenges when using mid-IR drivers is the reduction in total HHG flux. It may be experimentally possible to distinguish the super-Gaussian scaling due to the Lorentz drift in Eq. (8) from the polynomial scaling due to quantum diffusion, but would likely prove difficult. The quantum diffusion scaling is dominant and would obscure the Lorentz drift contribution.

The Lorentz displacement is also expected to affect the HHG spatial mode. It has been demonstrated that as the laser wavelength is increased, the HHG emission from only one $\frac{1}{2}$ -cycle of the driver is fully phase-matched [31], generating a single X-ray burst even for a multi-cycle driver. Therefore, for sufficiently long driving wavelengths and ideal phase-matching conditions, an isolated HHG pulse should be produced with an asymmetric mode profile along the polarization direction, as indicated by Fig. 6. Further, varying the intensity or carrier-envelope-phase (CEP) of the driving pulse can cause the particular $\frac{1}{2}$ -cycle that is

phase-matched to change, thus causing the asymmetric HHG mode to flip about the x-axis. Imaging this mode onto an X-ray CCD camera and adjusting the intensity or CEP could reveal a signature of the spatially-dependent Lorentz drift. In contrast, for the lower photon energy range where multiple $\frac{1}{2}$ -cycles contribute to the HHG signal, a more symmetric mode is expected that could obscure the Lorentz drift signature, but a full spatio-temporal attosecond pulse characterization technique could be employed to reveal the spatio-temporal asymmetry [32].

When multiple $\frac{1}{2}$ -cycles of the driver contribute constructively to HHG, individual harmonics are spectrally resolved. Using single-color drivers, only odd order harmonics are observed due to the emission of HHG bursts every $\frac{1}{2}$ -cycle. This typical twice-per-cycle emission in the time domain causes the energy spacing of harmonics in the spectral domain to be twice the fundamental photon energy. Even harmonics are, therefore, not allowed. However, the Lorentz displacement can break the $\frac{1}{2}$ -cycle symmetry in some spatial regions, and thus give rise to even harmonics. Looking off-axis in Fig. 6, the recombination probability ratio is close to unity in the lower half of the mode (i.e. δ_{Ez} cancels $\delta_{v \times B}$). In the next $\frac{1}{2}$ -cycle, this spatial location will not experience the same drift cancellation due to the sign flip of δ_{Ez} , but not $\delta_{v \times B}$. At this spatial position, there will be bright emission, followed by weak emission during the next $\frac{1}{2}$ -cycle, and so on. A portion of this signal will have the usual $\lambda_L / 2$ periodicity, which produces odd harmonics. Additionally, there will be a portion that has a λ_L periodicity that will give rise to every harmonic, including the even orders. By analyzing the asymmetry of Fig. 6, it is possible to predict the mode profile of the even and odd harmonics. By using an imaging spectrometer that can separate the individual harmonics of a $10 \mu\text{m}$ driver near $1U_p$, one would expect to observe a signal similar to that shown in Fig. 7. Here, the peak intensity of the even harmonics is close to 30% that of the odd harmonics, but this ratio approaches unity as the driving wavelength and harmonic energy are increased (i.e. $20 \mu\text{m}$ and $2U_p$). Note that this result includes only the modulations in amplitude, and that $\frac{1}{2}$ -cycle phase asymmetries can shift the absolute spectral positions of the harmonics [28]. Experimentally, resolving the individual harmonics with such long driving wavelengths and large harmonic energies would prove to be difficult, but might be possible with the use of a Fourier transform spectrometer, similar to the one used in [31].

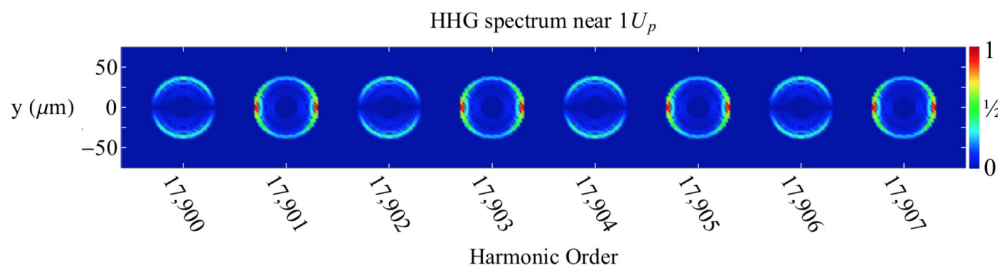


Fig. 7. Predicted HHG spectrum near $1U_p$ using a driving laser with $\lambda_L = 10 \mu\text{m}$, $w_L = 50 \mu\text{m}$, and $I_L = 2.77 \times 10^{14} \text{ W/cm}^2$. The moderate spatial and temporal asymmetry of the Lorentz drift gives rise to even harmonics with a two-lobed structure along the polarization direction.

7. Outlook

The laser modes and conditions presented in this paper have experimentally been the most successful for efficient HHG to date, but other modes could be considered. There are a number of low-loss waveguide modes other than the EH₁₁ mode, such as the TE or TM modes

that have interesting polarization properties and field components. The resulting interplay of these fields could show advantages with respect to harmonic flux.

Even considering the linearly-polarized EH_{nm} waveguide modes, it is possible to populate multiple modes at the same time, and the presence of the higher order modes could influence the drifts shown above. However, each mode propagates with a different phase velocity, so the resulting drift profiles would be changing with propagation. It could be possible to use this effect to implement quasi-phase-matching, periodically turning on and off the HHG process via the dynamic recombination probability ratio [33–35]. Furthermore, HHG driven by multiple wavelengths, circular polarizations, and noncollinear geometries can add other forms of control over the fields, and thus, the Lorentz drift.

Finally, this paper has investigated only the single-atom amplitude effects resulting from the Lorentz drift, but the quantum phase accumulated by the electron wavepacket during its trajectory should be influenced by the Lorentz force, and can have an effect on the phase-matching conditions as well as the spectrum. These phase effects will vary spatially and temporally, and combined with propagation, will modify the far field characteristics of the emitted harmonics. These phenomena will be discussed in future work.

8. Conclusions

We have presented a semi-classical analysis of the influence of the Lorentz force on efficient high harmonic generation and explored the resulting spatio-temporal effects. For finite laser modes, a longitudinal electric field component arises and contributes to the total Lorentz displacement of the ionized electron wavepacket. The drift resulting from the E_z field combines with the $\mathbf{v} \times \mathbf{B}$ drift to give a spatially-varying net drift profile, which can be close to zero over a relatively large area. Overall, the high harmonic flux gains an additional super-Gaussian scaling with wavelength, where noticeable attenuation occurs for driving wavelengths $> 6 \mu\text{m}$. Experimental signatures of the Lorentz drift include flux reduction, spatial mode shaping, and the emergence of even harmonics. Despite the reduction in flux, the Lorentz drift does not completely shut off harmonic emission, even for driving wavelengths $> 10 \mu\text{m}$ and recollision energies $> 15 \text{ keV}$.

Funding

Army Research Office (WN11NF-13-1-0259); Air Force Office of Scientific Research (AFOSR) Multidisciplinary University Research Initiative (MURI) (FA9550-16-1-0121); National Nuclear Security Administration (NNSA) Stewardship Science Graduate Fellowship (SSGF) (DE-NA0002135).

Acknowledgments

The authors wish to thank Carlos Hernández-García for the useful discussions and Seth Cousin for help with editing.